

Three-stage binarization of color document images based on discrete wavelet transform and generative adversarial networks

Rui-Yang Ju ^a, Yu-Shian Lin ^b, Yanlin Jin ^c, Chih-Chia Chen ^b, Chun-Tse Chien ^b and Jen-Shiun Chiang ^{b,*}

^aGraduate Institute of Networking and Multimedia, National Taiwan University, No. 1, Sec. 4, Roosevelt Rd., Taipei City, 106335, Taiwan

^bDepartment of Electrical and Computer Engineering, Tamkang University, No.151, Yingzhuang Rd., Tamsui Dist., New Taipei City, 251301, Taiwan

^cDepartment of Electrical and Computer Engineering, Rice University, 6100 Main St, Houston, 77005, Texas, USA

ARTICLE INFO

Keywords:

semantic segmentation
discrete wavelet transform
document enhancement
document image binarization
handwriting text recognition
generative adversarial networks

ABSTRACT

The efficient segmentation of foreground text information from the background in degraded color document images is a critical challenge in the preservation of ancient manuscripts. The imperfect preservation of ancient manuscripts has led to various types of degradation over time, such as staining, yellowing, and ink seepage, significantly affecting image binarization results. This work proposes a three-stage method using generative adversarial networks (GANs) for the degraded color document images binarization. Stage-1 involves applying discrete wavelet transform (DWT) and retaining the low-low (LL) subband images for image enhancement. In Stage-2, the original input image is split into red, green, and blue (RGB) three single-channel images and one grayscale image, and each image is trained with independent adversarial networks to extract color foreground information. In Stage-3, the output image from Stage-2 and the resized input image are used to train independent adversarial networks for document binarization, enabling the integration of global and local features. The experimental results demonstrate that our proposed method outperforms other traditional and state-of-the-art (SOTA) methods on the Document Image Binarization Contest (DIBCO) datasets. We have released our implementation code at <https://github.com/abcpp12383/ThreeStageBinarization>.

1. Introduction

Historical analysis of human societies primarily relies on reconstructing and analyzing preserved ancient documents. Parchment manuscripts and paintings have predominantly served as the means of preserving crucial ancient documents throughout the evolution of human society. Analyzing preserved ancient documents presents challenges due to potential forms of interference and degradation, including paper yellowing, text fading, page contamination and moisture damage.

Document image enhancement is one of the most important tasks in the reconstruction and analysis of ancient documents. It involves the document image binarization to extract essential text information from the page. Elevating the image quality of deteriorated documents necessitates addressing various challenges, including text degradation and bleed-through issues, such as text degradation and bleed-through [1, 2, 3, 4]. However, traditional binarization methods struggle to extract text information from the background of degraded documents effectively, often resulting in incomplete removal of shadows and noises, or loss of text information.

With the development of deep learning, neural networks have been applied to image binarization. Calvo-Zaragoza

and Gallego [5] introduced a selectional auto-encoder approach, parsing the text through the trained network model, and performing binarization using threshold. Fully convolutional network (FCN) [6, 7] enables the generated images to maintain the same size as the input images, and the task of generating document binarization using FCN [8] is also included in the semantic segmentation task. However, most image binarization methods primarily process grayscale documents, targeting contaminated black and white scanned ancient documents as their default.

Considering that some scanned images of ancient documents are in color, we propose a novel generative adversarial network framework for document image enhancement and color degraded documents binarization [9]. The proposed method consists of three stages. In Stage-1, we split the original input image into red, green, and blue (RGB) three single-channel images and one grayscale image, and apply discrete wavelet transform (DWT) to retain the low-low (LL) subband images and normalize them to achieve image enhancement. In Stage-2, we train four independent adversarial networks with the four single-channel images to eliminate background information and extract color foreground details from the local image patches. During the processing of Stage-3, the multiscale adversarial networks produce 224×224 image patch (local) prediction outputs and 512×512 resized image (global) prediction outputs for the document images, which are subsequently fused to obtain the final output.

To evaluate the performance of the proposed method for degraded document image binarization, we compare it with

*Corresponding author: jksen.chiang@gmail.com

jryjry1094791442@gmail.com (Rui-Yang Ju); abcp12383@gmail.com (Yu-Shian Lin); neil.yl.jin@gmail.com (Yanlin Jin); crystal88irene@gmail.com (Chih-Chia Chen); popper0927@hotmail.com (Chun-Tse Chien); jksen.chiang@gmail.com (Jen-Shiun Chiang)

ORCID(s): 0000-0003-2240-1377 (Rui-Yang Ju); 0000-0001-9825-9958 (Yu-Shian Lin); 0000-0001-8466-0660 (Yanlin Jin); 0000-0003-0848-9747 (Chih-Chia Chen); 0009-0008-7549-4021 (Chun-Tse Chien); 0000-0001-7536-8967 (Jen-Shiun Chiang)

other methods using DIBCO datasets of 2011, 2013, 2014, 2016, 2017, and 2018 [10, 11, 12, 13, 14, 15].

The main contributions of this paper are as follows:

- Introducing a novel three-stage generative adversarial networks method for enhancing and binarizing the degraded color documents.
- The incorporation of discrete wavelet transform prior to the training of generative adversarial networks stands as a pivotal innovation, enhancing model performance when compared to the baseline model.
- The proposed method achieves the state-of-the-art performance on multiple benchmark datasets.

The rest of this paper is organized as follows: Section 2 describes the deep learning method for document image binarization. Section 3 introduces a novel three-stage generative adversarial networks method. Section 4 presents the comparison experiment and the ablation study, and compares the performance of our method and other methods on several benchmark datasets. Finally, Section 5 discusses the conclusion and the future work of this paper.

2. Related Work

In previous researches focusing on document image binarization, the field is broadly divided into two categories: traditional image processing methods and deep learning-based semantic segmentation methods. However, traditional image processing binarization methods are always based on the pixel-level local threshold values, such as global binarization [16] and local adaptive binarization [17, 18]. These methods are not satisfactory when dealing with documents affected by excessive interference or degradation.

With the advancement of deep learning, the convolutional neural network (CNN) framework [19, 20] has become the predominant backbone of computer vision tasks. Within computer vision, semantic segmentation [7] is one of the most important research topics, encompassing document image binarization. For instance, Tensmeyer *et al.* [8] employed pseudo-F-measure (p-FM) and F-measure (FM) loss during the training of FCN to apply the model to the document image binarization task. Ronneberger *et al.* [21] extended FCN, presenting the U-Net architecture, which captures contextual and spatial information through its distinctive U-shaped design. Inspired by this, Peng *et al.* [22] introduced an encoder-decoder architecture for document image binarization, where the decoder transforms the low-resolution representation to the original dimensions, resulting in the binarized image. Vo *et al.* [23] first applied hierarchical deep supervised network (DSN) to document image binarization and achieved the state-of-the-art (SOTA) performance on several benchmark datasets. He *et al.* [24] proposed an iterative deep learning framework applied to document image binarization and the trained model achieved excellent performance.

In recent years, generative adversarial networks (GANs) [25] have achieved exciting results [26, 27] in the generation of real-world images. Unlike GANs which generate output images from random noise, Isola *et al.* [28] proposed Pix2Pix GAN based on conditional GAN (cGAN) [29] for image-to-image translation. To ensure that the generated images are more realistic, Pix2Pix GAN employs generators for loss function optimization. Within the network architecture, the generator evaluates the minimized generated image against the target output image, quantifying the $L1$ loss between them. Meanwhile, the discriminator assesses the credibility of the generated image, relying on the input image and the reference target image. This process is depicted by the subsequent equation:

$$\arg \min_G \max_D V(G, D) = \mathbb{E}_x[\log(1 - D(x, G(x)))] + \mathbb{E}_{x,y}[\log D(x, y)] + \lambda \mathbb{E}_{x,y}[\|y - G(x)\|_1] \quad (1)$$

where the input data distribution \mathbb{P}_x samples the input image x ; the ground truth image of the input image is y , and the hyperparameter to increase the model regularization effect is λ . Generator G generates the input image as the generated image $G(x)$. From Eq. (1), the loss function between the generated image and the ground truth image is $L1$ instead of $L2$, which is beneficial to reduce blurring and ambiguity in the generation process.

Bhunua *et al.* [30] performed document image enhancement on the dataset [10, 11, 12, 13, 14, 15] and used cGAN [29] for image binarization. Inspired by Pix2Pix GAN [28], Zhao *et al.* [31] proposed a cascade generator structure for document image binarization based on Pix2Pix GAN to solve the problem of multi-scale information combination. De *et al.* [32] designed two discriminators to combine local and global information. Suh *et al.* [33] set up a two-stage generative adversarial network for image binarization using Patch GAN [28]. Nicolaou *et al.* [34] proposed the TorMentor image enhancement framework by adapting global image enhancement transformations to continuous local transformations using plasma fractals. Souibgui *et al.* [35] proposed a new encoder-decoder architecture based on visual converters for enhancing machine printed and handwritten document images. These methods keep breaking the SOTA performance on DIBCO datasets.

3. Proposed Method

3.1. Overall Network Architecture

The aim of this work is to enhance image quality in the context of degraded color documents and extract text information from these document images. Since the degradation of color document images is diverse and complex, which requires processing of images with different color channels, our proposed method divides the overall network architecture into three stages. In Stage-1, we use DWT and normalization to preprocess the patches of the input image. These preprocessed image patches are employed to train as the input of the generator within the adversarial network

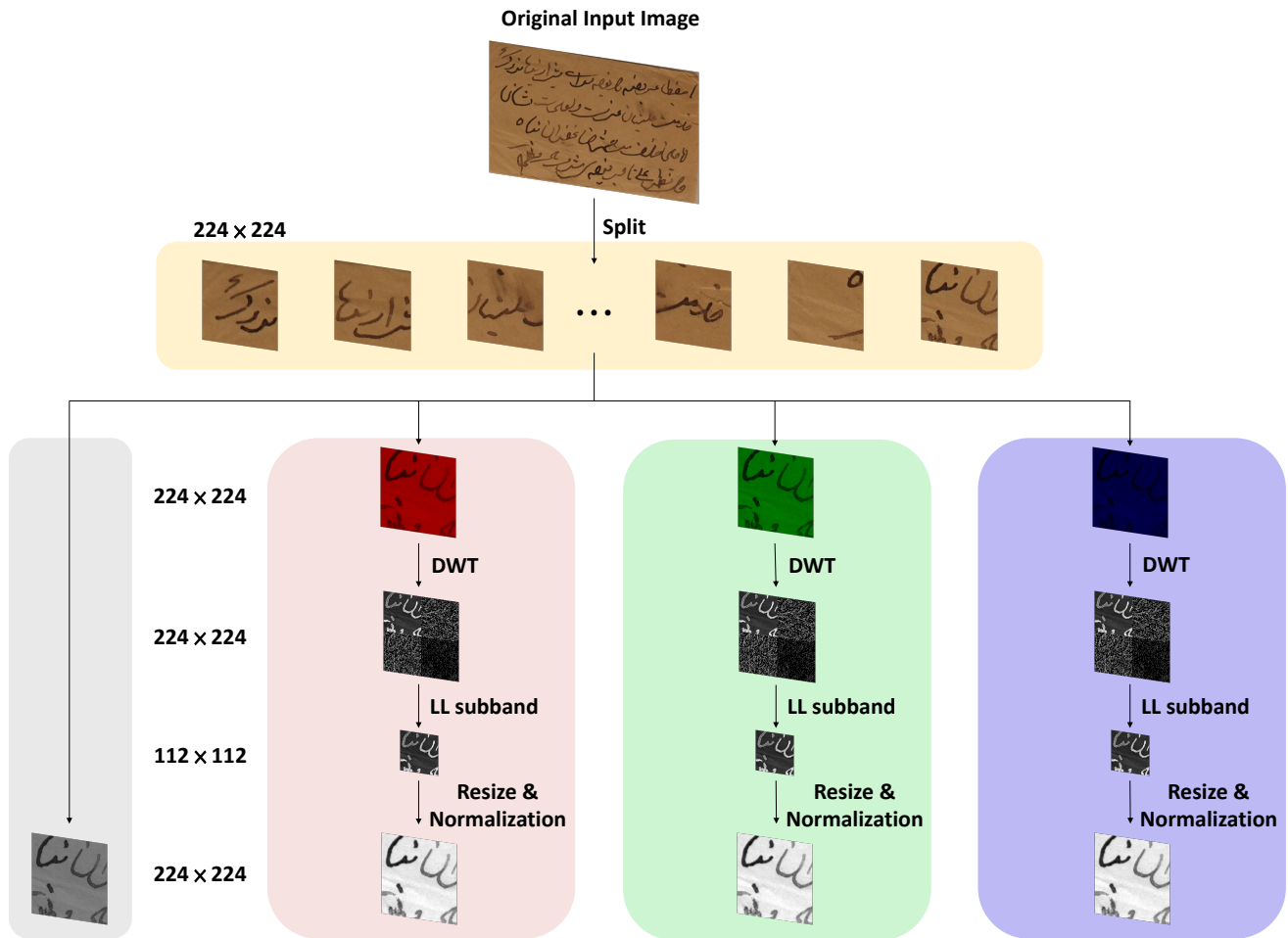


Figure 1: The architecture diagram of stage-1 of the proposed method. The original input image is divided into patches of 224×224 size, and split into RGB three single-channel images and one grayscale image for the discrete wavelet transform (DWT) and the normalization.

framework. Stage-2 focuses on the elimination of background color noise and the extraction of color foreground information, while Stage-3 involves the fusion of local and global predictions to produce the final output. The detailed introduction of each stage can be found in Sections 3.2, 3.3, and 3.4, respectively.

3.2. Stage-1

This work employs four different generators to extract foreground color information from degraded document images while eliminating the background color. To preprocess the input of the different generators, we first split the original color image (24-bit) into RGB three single-channel images (8-bit) and one grayscale image (8-bit).

The ground truth (GT) image provided by the dataset is a single-channel grayscale binary image (8-bit), where pixel points have values of 0 for characters and 1 for the background. Images with varying channel numbers cannot be directly put into the discriminator for processing. As shown in Figure 1, we first split the RGB three channels

of the original input image to create three single-channel RGB images. Then we apply DWT to each single-channel image, and retain the LL subband images for normalization. The GT images and the preprocessed grayscale images are summed at pixel wise as the corresponding ground truth images. Since the sizes of the retained LL subband images are 112×112 (half of the 224×224 length and width), we resize the images to the designated size of 224×224 using bicubic interpolation [36].

3.2.1. Discrete Wavelet Transform

In this work, we use haar wavelet transform [37, 38], which is one of the DWTs, to process the input image. This process can be conceived as a bandpass filter, selectively allowing signals with frequencies akin to those of the wavelet basis function to traverse. The flowchart of this DWT processing is illustrated in Figure 2. Given single-channel split images as input, the initial step involves processing the n -direction through high pass, low pass, and frequency reduction operations. This results in an image

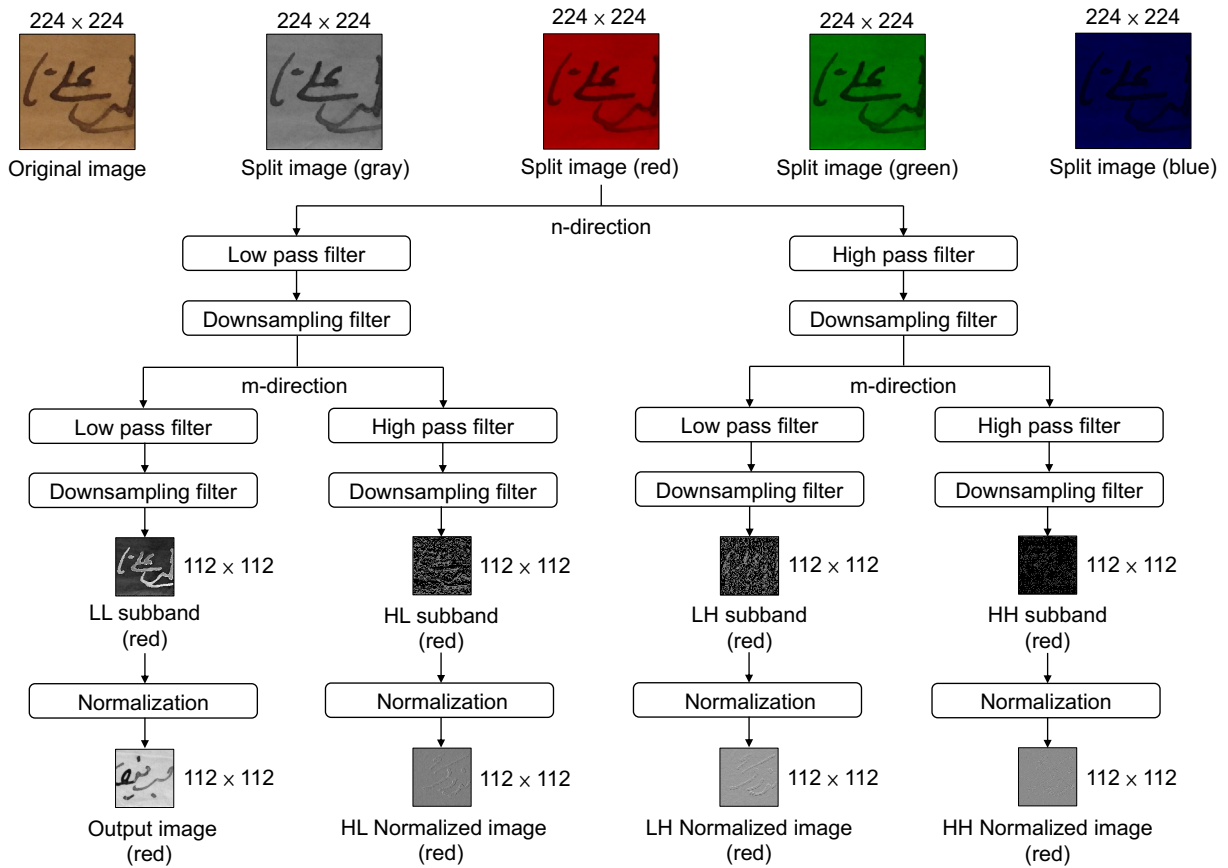


Figure 2: The architecture diagram of the haar wavelet transform used by the proposed method, which takes the red single-channel image patch as an example, and the transform processes of the green and blue single-channel image patches are the same.

| | LL Normalized Image | HL Normalized Image | LH Normalized Image | HH Normalized Image |
|-------|---------------------|---------------------|---------------------|---------------------|
| Gray | | | | |
| Red | | | | |
| Green | | | | |
| Blue | | | | |

Figure 3: Example of the result of haar wavelet transform and normalization of RGB single-channel images and the grayscale image split from the image patch.

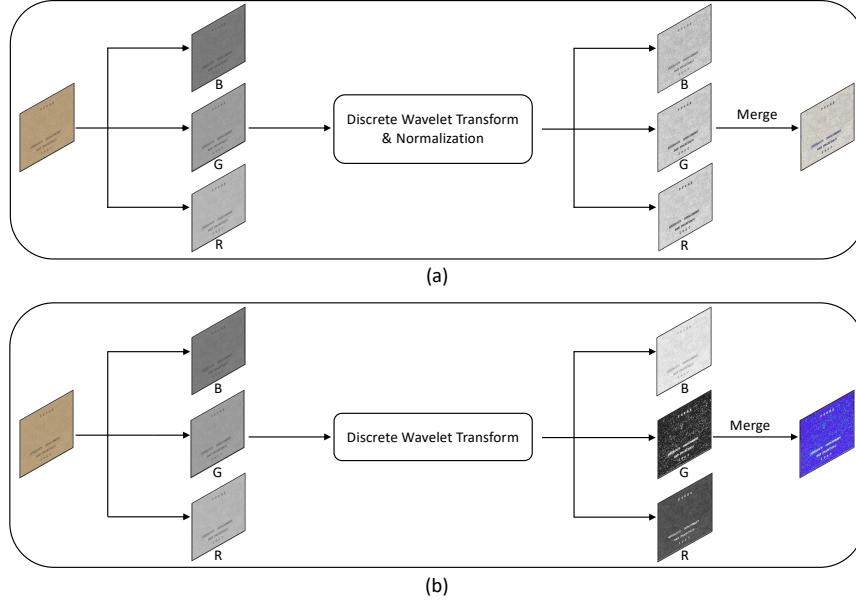


Figure 4: Example of image normalization from image HW15 of DIBCO 2011 dataset: (a) Normalization after DWT retains LL subband images, (b) No normalization after DWT retains LL subband images.

comprising low-frequency composition on the left and high-frequency composition on the right. The equation for the one-dimensional DWT is shown below:

$$v_L[m, n] = \sum_{k=0}^{K-1} x[m, 2n - k]g[k] \quad (2)$$

$$v_H[m, n] = \sum_{k=0}^{K-1} x[m, 2n - k]h[k]$$

High-pass, low-pass, and frequency reduction operations can be applied to Eq. (2) in the m -direction, resulting in the following equations:

$$v_{LL}[m, n] = \sum_{k=0}^{K-1} v_L[2m - k, n]g[k]$$

$$v_{HL}[m, n] = \sum_{k=0}^{K-1} v_L[2m - k, n]h[k] \quad (3)$$

$$v_{LH}[m, n] = \sum_{k=0}^{K-1} v_H[2m - k, n]g[k]$$

$$v_{HH}[m, n] = \sum_{k=0}^{K-1} v_H[2m - k, n]h[k]$$

The application of the DWT generates four subband images: one low-frequency subband image and three high-frequency subband images.

In contrast to the ground truth images provided by the dataset, the RGB single-channel images split from the original input images exhibit substantial noise. This noise prevents them from being used directly in generating corresponding ground truth images through the generator and

could potentially disrupt the performance of the trained adversarial network. The DWT decomposes the image into both low-frequency and high-frequency information. The low-frequency component represents the mean value and the high-frequency component represents the difference value. The mean value, classified as low-frequency information, captures gradual changes and encodes both the picture's contour information and approximate details. Conversely, the difference value, characterized as high-frequency information, captures rapid changes and encodes intricate picture details as well as local information (including noise). Therefore, we apply the DWT and retain the LL subband images to input Stage-2, as shown in Figure 2. This decision effectively preserves contour information and reduces noise interference.

3.2.2. Normalization

Normalization entails constraining data within a desired range, with the goal of simplifying the data processing and expediting convergence. The proposed equation for this process is expressed as:

$$I_N = (IV_{\text{max}} - IV_{\text{min}}) \frac{1}{1 + e^{-\frac{I - \beta}{\alpha}}} + IV_{\text{min}} \quad (4)$$

where IV is the intensity values, the image to be processed $I : \{\mathbb{X} \subseteq \mathbb{R}^n\} \rightarrow \{IV_{\text{min}}, \dots, IV_{\text{max}}\}$, and the generated image $I_N : \{\mathbb{X} \subseteq \mathbb{R}^n\} \rightarrow \{IV_{\text{min}}, \dots, IV_{\text{max}}\}$. α defines the width of the input intensity range, and β defines the range centered intensity.

In our method, we normalize the LL subband images to present initially incomparable data for comparison. The reason we choose the normalized LL subband image as the

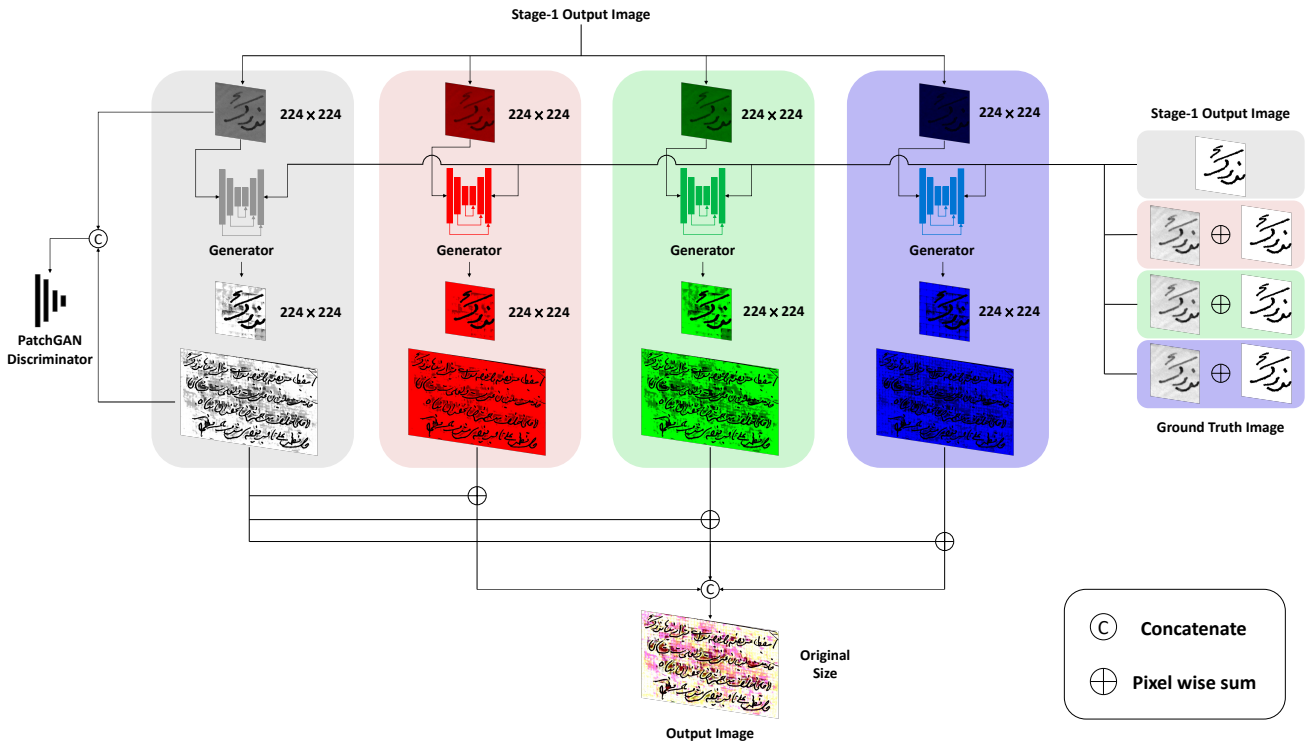


Figure 5: The architecture diagram of stage-2 of the proposed method. This method employs the U-Net++ architecture with EfficientNet as the generator and PatchGAN as the discriminator. The ground truth image during the training process is derived through pixel-wise summation of the dataset provided image and the output from stage-1.

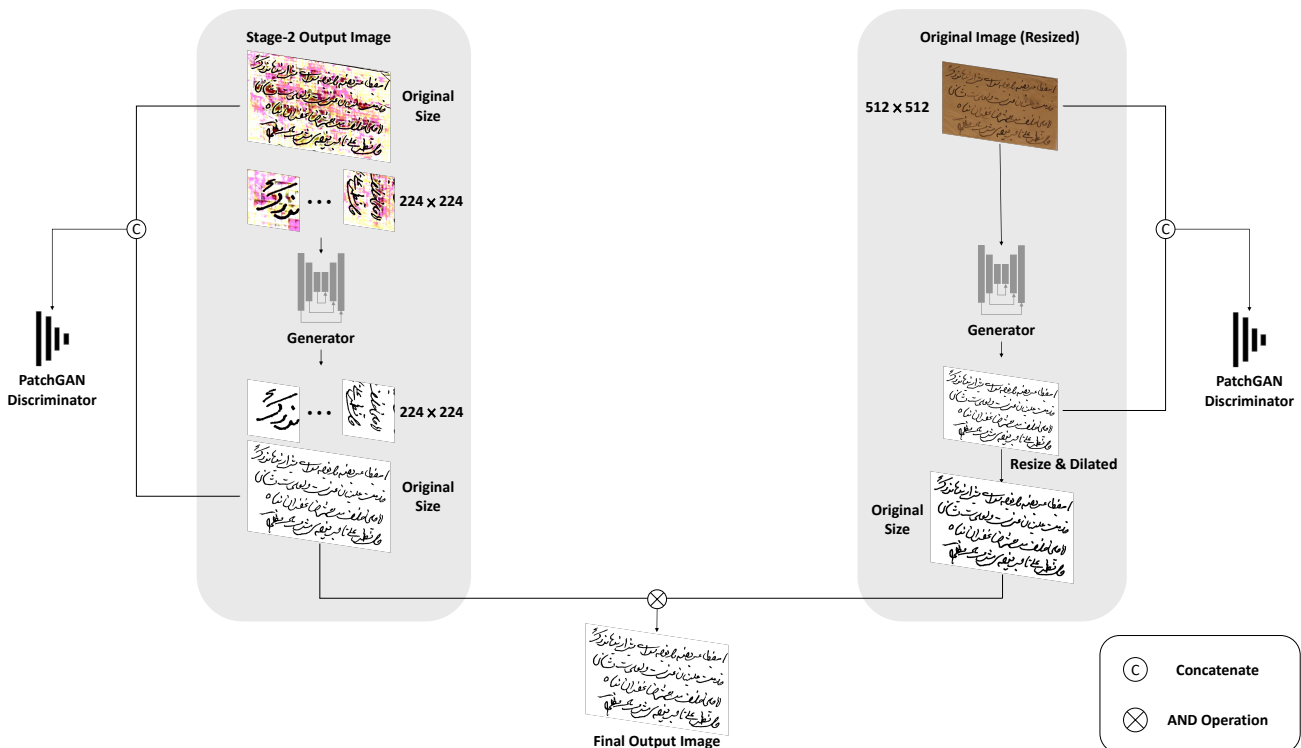


Figure 6: The architecture diagram of stage-3 of the proposed method. This stage comprises both local and global predictions. The local prediction involves training several 224×224 image patches, while the global prediction involves directly resizing the original image to 512×512 for training.

output is shown in Figure 3, where we apply DWT and normalization to each subband images.

The illustrative example of the impact of normalization on RGB single-channel images after the DWT operation is provided in Figure 4, when applied to image HW15 from the DIBCO 2011 dataset, normalization effectively balances the RGB. In contrast, not applying normalization results in an output image, it heavily skews towards the blue component. A comprehensive investigation into the influence of normalization on experimental outcomes is expounded upon in the comparative experiment outlined in Section 4.6.

3.3. Stage-2

In Stage-2, the proposed method is illustrated in Figure 5. Initially, the original input images are split into three RGB single-channel images and one grayscale image. Each of the single-channel images is processed by an independent generator. Furthermore, a shared discriminator is employed across all the single-channel images to differentiate between the generated images and their corresponding ground truth.

The four generators are individually trained using different single-channel images. Therefore, the trained adversarial networks have the capability to eliminate background information from localized image blocks while simultaneously extracting the colored foreground details.

3.3.1. Network architecture

The generator employs an encoder-decoder architecture, utilizing the U-Net++ framework [39, 40]. Within the generator, the encoders serve to extract features, while a shared encoder is employed alongside multiple decoders of varying depths, and subsequently the features are concatenated. The encoder facilitates downsampling and context extraction, while the decoders undertake upsampling and amalgamate both upscaled and downsampled features. In our method, we use EfficientNet [41] as the encoder, which is a lightweight CNN recognized for its strong performance in image classification tasks. To enhance generalization, the discriminator within the network architecture is upgraded following the principles of PatchGAN [42, 43, 44].

Given the unpredictability of color document degradation, this work adopts four independent adversarial networks to extract text information from diverse colored backgrounds. This method mitigates color interference during document image binarization.

3.3.2. Loss functions of GAN

To ensure a more robust convergence of the loss function, we employ the Wasserstein generative adversarial network with gradient penalty (WGAN-GP) [45] on the objective function. Empirical investigations conducted by Bartuskiak *et al.* [46] have demonstrated that the binary cross-entropy (BCE) loss yields superior performance compared to the $L1$ loss in binary classification tasks. Therefore, we opt for the utilization of the BCE loss instead of the $L1$ loss used in the Pix2Pix GAN framework [28]. The loss function of the WGAN-GP target, which incorporates the BCE loss,

Algorithm 1 Training process for GAN

Require: Adam optimizer, $\eta = 1 \times 10^{-4}$

Ensure: $\omega = 0.5$, $\alpha = 10$, $\lambda = 50$

```

1: Initialize: Parameters  $\theta_{G_r}, \theta_{G_g}, \theta_{G_b}, \theta_{G_{gray}}$ 
2: for number of training iterations do
3:   Input Image Split into  $r, g, b, gray$  images
4:   for  $k = \{r, g, b, gray\}$  do
5:     if  $k$  is gray then
6:        $y_k \leftarrow y$ 
7:     else
8:        $x'_k = Norm(V_{LL}(x_k))$ 
9:        $y_k \leftarrow x'_k \cap y$ 
10:      Binarize  $y_k$  with threshold value  $t$ .
11:    end if
12:    Update Discriminator  $D$  (Eq. (5)):
13:     $\theta_D \leftarrow \theta_D - \eta_D \nabla_{\theta_D} \mathbb{L}_D$ 
14:    Update Generator  $G_k$  (Eq. (6)):
15:     $\theta_{G_k} \leftarrow \theta_{G_k} - \eta_G \nabla_{\theta_{G_k}} \mathbb{L}_G$ 
16:  end for
17: end for
18: for  $k = \{r, g, b\}$  do
19:    $\hat{y}_k \leftarrow \omega G_k(x_k) + (1 - \omega)G_{gray}(x_{gray})$ 
20: end for
21:  $\hat{y} \leftarrow [\hat{y}_r, \hat{y}_g, \hat{y}_b]$ 

```

is formulated as follows:

$$\mathbb{L}_D = -\mathbb{E}_{x,y}[D(y,x)] + \mathbb{E}_x[D(G(x),x)] + \alpha \mathbb{E}_{x,\hat{y} \sim P_{\hat{y}}}[(\|\nabla_{\hat{y}} D(\hat{y},x)\|_2 - 1)^2] \quad (5)$$

$$\mathbb{L}_G = \mathbb{E}_x[D(G(x),x)] + \lambda \mathbb{E}_{G(x),y}[y \log G(x) + (1-y) \log(1-G(x))] \quad (6)$$

where the penalty coefficient is α , and the uniform sampling along a straight line between the ground truth distribution P_y and the point pairs of the generated data distribution is $P_{\hat{y}}$. λ is used to control the relative importance of different loss terms. The parameter of the generator is θ_G and the parameter of the discriminator is θ_D . In the discriminator, the generated image is distinguished from the real image by the target loss function \mathbb{L}_D in Eq. (5). In the generator, the distance between the generated image and the ground truth image in each color channel is minimized by the target loss function \mathbb{L}_G in Eq. (6).

The detailed procedure for training GAN models is illustrated in Algorithm 1. The training process is conducted within a specially designed environment, encompassing optimizer selection, learning rate configuration, and loss function definition. The algorithm demonstrates that the GAN model iteratively updates the loss function based on the authenticity assessment of the generated image by the discriminator. This iterative process enhances the ability of the generator to produce more realistic images.



Figure 7: Examples of document images enhancement and binarization in the DIBCO dataset: (a) the original input image, (b) the LL subband image obtained by applying discrete wavelet transform and normalization (Stage-1), (c) the enhanced image produced using our image enhancement method (Stage-2), (d) the binarized image obtained by combining local and global predictions (Stage-3), (e) the ground truth image.

3.4. Stage-3

In Stage-3, a multi-scale adversarial network is employed to generate images for both local and global binarization results, enhancing the distinction between the background and text with higher accuracy. Contrary to Stage-2, which predominantly relies on local prediction using the image patches (224×224), Stage-3 conducts global prediction on the resized input image (512×512). This method reduces the contextual information loss in text caused by the local predictions of Stage-2. Figure 6 illustrates the process of two independent discriminators in Stage-3. Different from Stage-2 using 8-bit images for local prediction, Stage-3 uses 24-bit images as the input of the generator. Additionally, Figure 6 clarifies that the left-side input image comprises the image patches from the Stage-2 output, intended for local prediction. Conversely, the right-side input image represents the resized image from the original input for global prediction. In the binarization process of Stage-3, the network architecture of the generator remains consistent with Stage-2, differing only in the number of input channels.

4. Experiments

4.1. Datasets

We compared the proposed method with traditional and SOTA methods on multiple public datasets. For the training set, we selected the images from DIBCO 2009 [47], H-DIBCO 2010 [48], Persian Heritage Image Binarization Dataset (PHIBD) [49], H-DIBCO 2012 [50], Synchronmedia Multispectral Ancient Document Images Dataset (SMADI) [1], Bickley Diary Dataset [51], and Shipping Label Image Dataset [52]. Additionally, the test sets consist of the images from DIBCO 2011 [10], DIBCO 2013 [12], H-DIBCO 2014 [11], H-DIBCO 2016 [13], DIBCO 2017 [15], and H-DIBCO2018 [14]. In summary, a total of 82 images are used for testing.

4.1.1. DIBCO

The Document Image Binarization Competition (DIBCO) provides several datasets: DIBCO 2009, H-DIBCO 2010, DIBCO 2011, H-DIBCO 2012, DIBCO 2013, DIBCO 2017, H-DIBCO 2014, H-DIBCO 2016, and H-DIBCO 2018.

Table 1

Comparison experiment of input image and ground truth (GT) image using discrete wavelet transform (DWT) and normalization.

| (a) DIBCO 2011 | | | | | | (b) DIBCO 2013 | | | | | |
|----------------|----------|---------------|-----------------|-----------------|------------------|----------------|----------|---------------|-----------------|-----------------|------------------|
| Input | GT | FM \uparrow | p-FM \uparrow | PSNR \uparrow | DRD \downarrow | Input | GT | FM \uparrow | p-FM \uparrow | PSNR \uparrow | DRD \downarrow |
| Original | Original | 86.68 | 89.61 | 19.27 | 4.01 | Original | Original | 92.94 | 94.70 | 21.57 | 2.74 |
| Original | DWT | 88.20 | 90.57 | 19.53 | 3.45 | Original | DWT | 94.43 | 95.64 | 21.79 | 2.13 |
| Original | DWT+Norm | 87.70 | 90.24 | 19.65 | 3.45 | Original | DWT+Norm | 94.88 | 96.19 | 22.32 | 1.95 |
| DWT | Original | 87.74 | 89.69 | 18.88 | 3.78 | DWT | Original | 93.23 | 94.43 | 20.80 | 2.67 |
| DWT+Norm | Original | 89.33 | 91.94 | 19.49 | 3.37 | DWT+Norm | Original | 93.76 | 95.41 | 21.54 | 2.40 |
| DWT | DWT | 90.53 | 92.82 | 19.68 | 3.11 | DWT | DWT | 94.39 | 95.34 | 21.91 | 2.26 |
| DWT+Norm | DWT+Norm | 89.06 | 92.25 | 19.59 | 3.31 | DWT+Norm | DWT+Norm | 94.55 | 95.86 | 22.02 | 2.07 |

| (c) H-DIBCO 2014 | | | | | | (d) H-DIBCO 2016 | | | | | |
|------------------|----------|---------------|-----------------|-----------------|------------------|------------------|----------|---------------|-----------------|-----------------|------------------|
| Input | GT | FM \uparrow | p-FM \uparrow | PSNR \uparrow | DRD \downarrow | Input | GT | FM \uparrow | p-FM \uparrow | PSNR \uparrow | DRD \downarrow |
| Original | Original | 96.50 | 97.50 | 22.08 | 1.01 | Original | Original | 90.74 | 94.46 | 19.39 | 3.30 |
| Original | DWT | 96.52 | 97.70 | 22.15 | 0.99 | Original | DWT | 91.76 | 95.74 | 19.67 | 2.93 |
| Original | DWT+Norm | 96.88 | 98.03 | 22.68 | 0.89 | Original | DWT+Norm | 91.49 | 96.46 | 19.68 | 2.92 |
| DWT | Original | 95.94 | 96.91 | 21.31 | 1.19 | DWT | Original | 91.86 | 94.95 | 19.62 | 2.99 |
| DWT+Norm | Original | 96.29 | 97.48 | 22.05 | 1.16 | DWT+Norm | Original | 91.28 | 96.03 | 19.47 | 3.04 |
| DWT | DWT | 96.60 | 97.60 | 22.27 | 0.97 | DWT | DWT | 91.68 | 95.90 | 19.68 | 2.93 |
| DWT+Norm | DWT+Norm | 96.77 | 97.89 | 22.52 | 0.91 | DWT+Norm | DWT+Norm | 91.95 | 95.87 | 19.75 | 2.84 |

These datasets comprise both grayscale and color images, including machine-printed as well as handwritten content. Participants in the competition were tasked with designing algorithms capable of extracting binarized text images from both handwritten and machine-printed images within these datasets.

4.1.2. PHIBD

The Persian Heritage Image Binarization Dataset (PHIBD) contains 15 images of historical manuscripts from Mirza Mohammad Kazemai's old manuscript library in Yazd, Iran. The images within the dataset have suffered from various types of degradation.

4.1.3. SMADI

The Synchronmedia Multispectral Ancient Document Images Dataset (SMADI) consists of 240 multispectral images of 30 authentic historical handwritten letters. These letters, dating from the 17th to the 20th centuries, were written using iron gall ink. The original documents are deposited at the BAnQ Bibliotheque et Archives nationales du Quebec. A total of 240 images of real documents were meticulously captured, calibrated, and registered within this dataset. Each of these images was imaged with a CROMA CX MSI camera, resulting in 8 images per document.

4.1.4. Bickley Diary Dataset

The Bickley Diary Dataset has been generously donated to the Singapore Methodist Archives by Erin Bickley. This dataset comprises diaries in which the images have been affected by both light and fold damages, thereby complicating the process of identification.

4.2. Shipping Label Image Dataset

The Shipping Label Image Dataset consists of 1,082 images of various types collected from different countries/regions using smartphones.

4.3. Evaluation Metric

In comparison with other traditional and SOTA methods for document image binarization, we use the following four evaluation metrics:

- 1) F-measure (FM):

$$FM = \frac{2 \times \text{Recall} \times \text{Precision}}{\text{Recall} + \text{Precision}} \quad (7)$$

where Recall is defined as $\frac{TP}{TP+FN}$; Precision is defined as $\frac{TP}{TP+FP}$, and TP, FP, and FN represent the true positive, false positive, and false negative values, respectively.

- 2) Pseudo-F-measure (p-FM):

$$p-FM = \frac{2 \times \text{Recall}_{ps} \times \text{Precision}_{ps}}{\text{Recall}_{ps} + \text{Precision}_{ps}} \quad (8)$$

where Pseudo-Recall (Recall_{ps}) and Pseudo-Precision (Precision_{ps}) both use the distance weights relative to the ground truth image profile to generate a new weighted ground truth image.

- 3) Peak signal-to-noise ratio (PSNR):

$$PSNR = 10 \log\left(\frac{V^2}{MSE}\right) \quad (9)$$

where V represents the difference between the foreground and background, and MSE (Mean Square Error) is defined as:

$$MSE = \frac{\sum_{x=1}^{width} \sum_{y=1}^{height} (L(x, y) - L'(x, y))^2}{width \times height} \quad (10)$$

Generally, a higher PSNR indicates greater similarity between the images.

Table 2

Performance evaluation of different methods for document binarization on DIBCO 2011. Best and 2nd best performance are in red and blue colors, respectively. Avg = (FM + p-FM + PSNR + (100-DRD)) /4.

| Method | Model | FM↑ | p-FM↑ | PSNR↑ | DRD↓ | Avg↑ |
|----------------------|--------------|-------|-------|-------|-------|-------|
| Niblack [17] | Thresholding | 70.44 | 73.03 | 12.39 | 24.95 | 57.73 |
| Otsu [16] | Thresholding | 82.10 | 85.96 | 15.72 | 8.95 | 68.71 |
| Sauvola et al. [18] | Thresholding | 82.35 | 88.63 | 15.75 | 7.86 | 69.72 |
| Vo et al. [53] | Thresholding | 88.20 | 90.30 | 20.10 | 2.00 | 74.15 |
| Howe [54] | Thresholding | 90.79 | 92.28 | 19.01 | 4.46 | 74.41 |
| Jia et al. [55] | Thresholding | 91.92 | 95.09 | 18.88 | 2.66 | 75.81 |
| Vo et al. [23] | CNN | 92.58 | 94.67 | 19.16 | 2.38 | 76.01 |
| He et al. [24] | CNN | 91.92 | 95.82 | 19.49 | 2.37 | 76.22 |
| Yang et al. [56] | CNN | 93.44 | 95.82 | 20.10 | 2.25 | 76.78 |
| Bhunia et al. [30] | CNN | 93.70 | 96.80 | 20.10 | 1.80 | 77.20 |
| Tensmeyer et al. [8] | CNN | 93.60 | 97.70 | 20.11 | 1.85 | 77.39 |
| Zhao et al. [31] | GAN | 92.62 | 95.38 | 19.58 | 2.55 | 76.26 |
| Suh et al. [27] | GAN | 93.44 | 96.18 | 19.97 | 1.93 | 76.92 |
| Suh et al. [33] | GAN | 93.57 | 95.93 | 20.22 | 1.99 | 76.93 |
| Ours | GAN | 94.97 | 98.25 | 20.70 | 1.68 | 78.06 |

Table 3

Performance evaluation of different methods for document binarization on DIBCO 2013. Best and 2nd best performance are in red and blue colors, respectively. Avg = (FM + p-FM + PSNR + (100-DRD)) /4.

| Method | Model | FM↑ | p-FM↑ | PSNR↑ | DRD↓ | Avg↑ |
|----------------------|--------------|-------|-------|-------|-------|-------|
| Niblack [17] | Thresholding | 71.38 | 73.17 | 13.54 | 23.10 | 58.75 |
| Otsu [16] | Thresholding | 80.04 | 83.43 | 16.63 | 10.98 | 67.28 |
| Sauvola et al. [18] | Thresholding | 82.73 | 88.37 | 16.98 | 7.34 | 70.19 |
| Howe [54] | Thresholding | 91.30 | 91.70 | 21.30 | 3.20 | 75.28 |
| Xiong et al. [57] | Thresholding | 93.50 | 94.40 | 21.30 | 2.70 | 76.63 |
| Vo et al. [23] | Thresholding | 93.43 | 95.34 | 20.82 | 2.26 | 76.83 |
| Jia et al. [55] | Thresholding | 93.28 | 96.58 | 20.76 | 2.01 | 77.15 |
| Tensmeyer et al. [8] | CNN | 93.10 | 96.80 | 20.70 | 2.20 | 77.10 |
| He et al. [24] | CNN | 93.36 | 96.70 | 20.88 | 2.15 | 77.20 |
| Yang et al. [56] | CNN | 95.19 | 96.37 | 22.58 | 1.78 | 78.09 |
| Zhao et al. [31] | GAN | 93.86 | 96.47 | 21.53 | 2.32 | 77.39 |
| Suh et al. [33] | GAN | 95.01 | 96.49 | 21.99 | 1.76 | 77.93 |
| Suh et al. [27] | GAN | 94.75 | 97.36 | 21.78 | 1.73 | 78.04 |
| Ours | GAN | 96.05 | 98.35 | 22.48 | 1.58 | 78.83 |

Table 4

Performance evaluation of different methods for document binarization on H-DIBCO 2014. Best and 2nd best performance are in red and blue colors, respectively. Avg = (FM + p-FM + PSNR + (100-DRD)) /4.

| Method | Model | FM↑ | p-FM↑ | PSNR↑ | DRD↓ | Avg↑ |
|---------------------|--------------|-------|-------|-------|------|-------|
| Niblack [17] | Thresholding | 86.01 | 88.04 | 16.54 | 8.26 | 70.58 |
| Sauvola et al. [18] | Thresholding | 83.72 | 87.49 | 17.48 | 5.05 | 70.91 |
| Otsu [16] | Thresholding | 91.62 | 95.69 | 18.72 | 2.65 | 75.85 |
| Jia et al. [55] | Thresholding | 94.89 | 97.68 | 20.53 | 1.50 | 77.90 |
| Howe [54] | Thresholding | 96.49 | 97.38 | 22.24 | 1.08 | 78.76 |
| Vo et al. [23] | CNN | 95.97 | 97.42 | 21.49 | 1.09 | 78.45 |
| He et al. [24] | CNN | 95.95 | 98.76 | 21.60 | 1.12 | 78.80 |
| Yang et al. [56] | CNN | 96.66 | 97.26 | 23.13 | 1.21 | 78.96 |
| Suh et al. [27] | GAN | 96.19 | 97.13 | 21.77 | 1.14 | 78.49 |
| Zhao et al. [31] | GAN | 96.09 | 98.25 | 21.88 | 1.20 | 78.76 |
| Suh et al. [33] | GAN | 96.36 | 97.87 | 21.96 | 1.07 | 78.78 |
| Ours | GAN | 97.45 | 98.95 | 22.49 | 0.94 | 79.49 |

Table 5

Performance evaluation of different methods for document binarization on H-DIBCO 2016. Best and 2nd best performance are in red and blue colors, respectively. Avg = (FM + p-FM + PSNR + (100-DRD)) / 4.

| Method | Model | FM↑ | p-FM↑ | PSNR↑ | DRD↓ | Avg↑ |
|---------------------|--------------|-------|-------|-------|-------|-------|
| Niblack [17] | Thresholding | 72.57 | 73.51 | 13.26 | 24.65 | 58.67 |
| Sauvola et al. [18] | Thresholding | 84.27 | 89.10 | 17.15 | 6.09 | 71.11 |
| Otsu [16] | Thresholding | 86.59 | 89.92 | 17.79 | 5.58 | 72.18 |
| Vo et al. [53] | Thresholding | 87.30 | 90.50 | 17.50 | 4.40 | 72.73 |
| Howe [54] | Thresholding | 87.47 | 92.28 | 18.05 | 5.35 | 73.11 |
| Bera et al. [58] | Thresholding | 90.43 | 91.66 | 18.94 | 3.51 | 74.38 |
| Jia et al. [55] | Thresholding | 90.10 | 93.72 | 19.00 | 4.03 | 74.70 |
| Vo et al. [23] | CNN | 90.01 | 93.44 | 18.74 | 3.91 | 74.57 |
| Yang et al. [56] | CNN | 90.41 | 94.70 | 19.00 | 3.34 | 75.19 |
| He et al. [24] | CNN | 91.19 | 95.74 | 19.51 | 3.02 | 75.86 |
| Kang et al. [59] | CNN | 93.09 | 94.85 | 19.18 | 3.03 | 76.02 |
| Bhunja et al. [30] | CNN | 92.30 | 95.40 | 19.90 | 2.70 | 76.23 |
| Zhao et al. [31] | GAN | 89.77 | 94.58 | 18.80 | 3.85 | 74.83 |
| Suh et al. [27] | GAN | 91.11 | 95.22 | 19.34 | 3.25 | 75.61 |
| Suh et al. [33] | GAN | 92.24 | 95.95 | 19.93 | 2.77 | 76.34 |
| Ours | GAN | 92.49 | 96.82 | 19.96 | 2.77 | 76.63 |

Table 6

Performance evaluation of different methods for document binarization on DIBCO 2017. Best and 2nd best performance are in red and blue colors, respectively. Avg = (FM + p-FM + PSNR + (100-DRD)) / 4.

| Method | Model | FM↑ | p-FM↑ | PSNR↑ | DRD↓ | Avg↑ |
|---------------------|--------------|-------|-------|-------|-------|-------|
| Otsu [16] | Thresholding | 77.73 | 77.89 | 13.85 | 15.54 | 63.48 |
| Sauvola et al. [18] | Thresholding | 77.11 | 84.10 | 14.25 | 8.85 | 66.65 |
| Bera et al. [58] | Thresholding | 83.38 | 89.43 | 15.45 | 6.71 | 70.39 |
| Jia et al. [55] | Thresholding | 85.66 | 88.30 | 16.40 | 7.67 | 70.67 |
| Howe [54] | Thresholding | 90.10 | 90.95 | 18.52 | 5.12 | 73.61 |
| Kang et al. [59] | CNN | 91.57 | 93.55 | 15.85 | 2.92 | 74.51 |
| Yang et al. [56] | CNN | 91.33 | 93.84 | 18.34 | 3.24 | 75.07 |
| Jemni et al. [60] | GAN | 89.80 | 89.95 | 17.45 | 4.03 | 73.29 |
| Zhao et al. [31] | GAN | 90.73 | 92.58 | 17.83 | 3.58 | 74.39 |
| Suh et al. [27] | GAN | 90.95 | 94.65 | 18.40 | 2.93 | 75.27 |
| Ours | GAN | 92.04 | 94.79 | 18.82 | 2.82 | 75.71 |

Table 7

Performance evaluation of different methods for document binarization on H-DIBCO 2018. Best and 2nd best performance are in red and blue colors, respectively. Avg = (FM + p-FM + PSNR + (100-DRD)) / 4.

| Method | Model | FM↑ | p-FM↑ | PSNR↑ | DRD↓ | Avg↑ |
|----------------------|--------------|-------|-------|-------|-------|-------|
| Otsu [16] | Thresholding | 51.45 | 53.05 | 9.74 | 59.07 | 38.79 |
| Sauvola et al. [18] | Thresholding | 67.81 | 74.08 | 13.78 | 17.69 | 59.50 |
| Jia et al. [55] | Thresholding | 76.05 | 80.36 | 16.90 | 8.13 | 66.30 |
| Bera et al. [58] | Thresholding | 76.84 | 83.58 | 15.31 | 9.58 | 66.54 |
| Howe [54] | Thresholding | 80.84 | 82.85 | 16.67 | 11.96 | 67.10 |
| Akbari et al. [61] | CNN | 89.05 | 93.65 | 19.17 | 4.80 | 74.27 |
| Kang et al. [59] | CNN | 89.71 | 91.62 | 19.39 | 2.51 | 74.55 |
| Yang et al. [56] | CNN | 91.09 | 94.57 | 19.92 | 3.07 | 75.63 |
| Souibgui et al. [35] | Transformer | 90.59 | 93.97 | 19.46 | 3.35 | 75.17 |
| Souibgui et al. [62] | GAN | 77.59 | 85.74 | 16.16 | 7.93 | 67.89 |
| Tamrin et al. [63] | GAN | 83.08 | 88.46 | 17.04 | 5.09 | 70.87 |
| Zhao et al. [31] | GAN | 87.73 | 90.60 | 18.37 | 4.58 | 73.03 |
| Jemni et al. [60] | GAN | 92.41 | 94.35 | 20.18 | 2.60 | 76.09 |
| Suh et al. [27] | GAN | 91.86 | 96.25 | 20.03 | 2.60 | 76.39 |
| Ours | GAN | 92.98 | 97.06 | 20.41 | 2.21 | 77.06 |

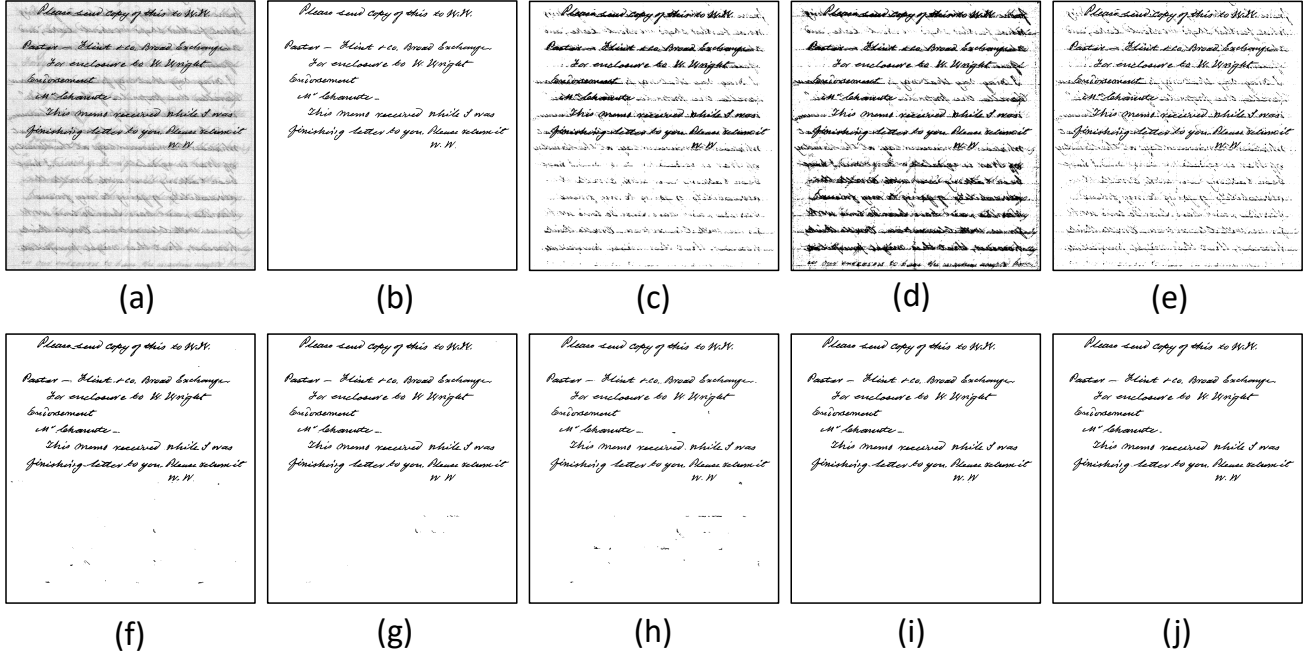


Figure 8: Example of document image binarization results from input image HW1 of DIBCO 2011 dataset by different methods: (a) original input images, (b) the ground truth, (c) Otsu [16], (d) Niblack [17], (e) Sauvola [18], (f) Vo [23], (g) He [24], (h) Zhao [31], (i) Suh [27], (j) Ours.

4) Distance reciprocal distortion (DRD):

$$\text{DRD} = \frac{\sum_k \text{DRD}_k}{\text{NUBN}} \quad (11)$$

where DRD_k is defined as:

$$\text{DRD}_k = \sum_{i=-2}^2 \sum_{j=-2}^2 |G_k(i, j) - B_k(x, y)| \times N_w(i, j) \quad (12)$$

where DRD represents a measure of visual distortion in the binary image. NUBN corresponds to the number of uneven 8×8 blocks in the ground truth image, while DRD_k indicates the distortion of the k_{th} flipped pixel, calculated using a 5×5 normalized weight matrix N_w . B_k refers to the pixel of the binary image, and G_k denotes the pixel of the ground truth image.

4.4. Implementation Details

The experiments were conducted using the PyTorch framework in Python. We use a single NVIDIA RTX 3090 GPU to complete the comparison experiments. For the ablation study and training process, we deploy our model on multiple NVIDIA A100 Tensor GPUs.

4.4.1. Data preparation

To ensure a fair comparison of performance among all methods, we used the same data augmentation for our method and other SOTA methods. During the training process of the local prediction network, this work splits the

input images into patches with 224×224 in size. These patches were sampled with scale factors of 0.75, 1.25, 1.5, subsequently resized to 224×224 , and rotated by 270° . This data augmentation process generated a total of 336,702 training image patches from the dataset. In contrast, for training the global prediction network, this work employed scaling without rotation for data augmentation, using a scaling size of 512×512 . To diversify the training data, rotation augmentation was applied to the global prediction, involving rotations of 90° , 180° , and 270° , as well as horizontal and vertical flips. This data augmentation process resulted in a set of 1,890 training image patches.

4.4.2. Training

The training parameters for Stage-2 and Stage-3 were consistent, differing solely in the number of training epochs: 150 epochs for global prediction and 10 epochs for the remaining networks. The choice of optimizer was Adam [64], with a learning rate set at 2×10^{-4} . Additionally the generator employed $\beta_1 = 0.5$, while the discriminator used $\beta_2 = 0.999$.

4.4.3. Pre-training

To enhance training efficacy due to limited data availability, we employed EfficientNet [41] as the encoder in the generator, utilizing weights pretrained on the ImageNet dataset [65].

4.5. Comparison with other Methods

Our proposed method was evaluated in the DIBCO datasets, and four evaluation metrics are presented in Section

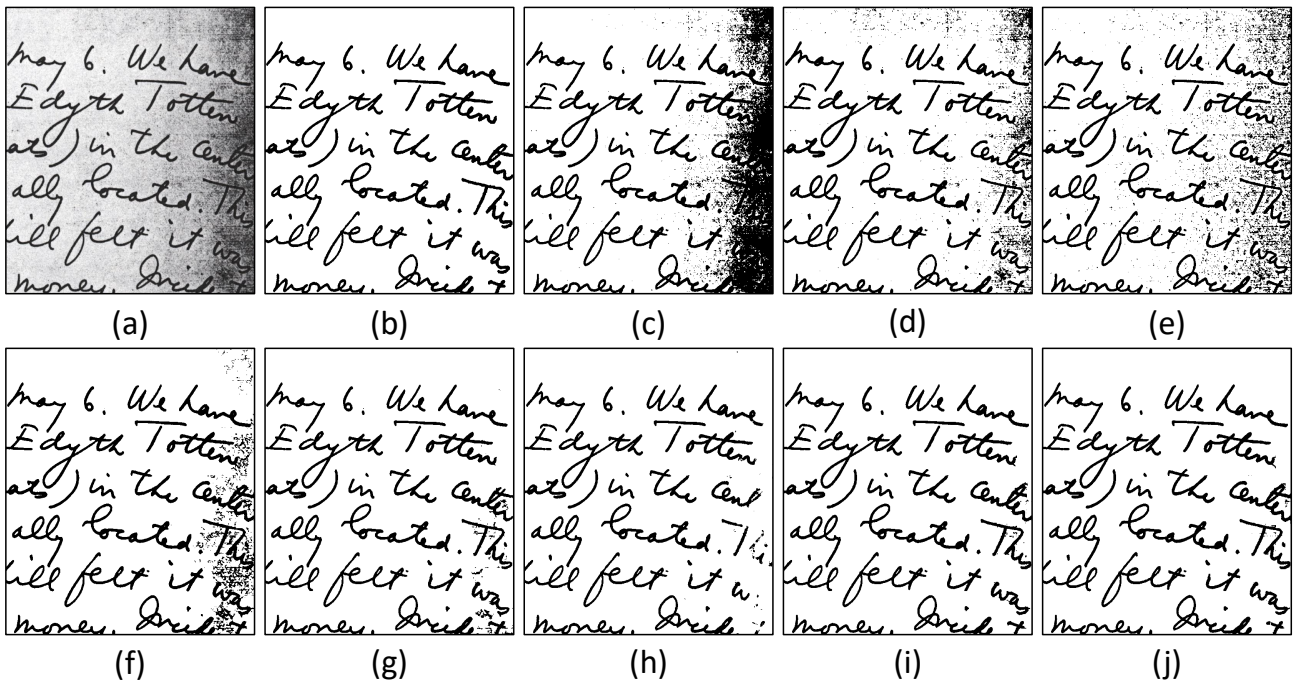


Figure 9: Example of document image binarization results from input image HW5 of DIBCO 2013 dataset by different methods: (a) original input images, (b) the ground truth, (c) Otsu [16], (d) Niblack [17], (e) Sauvola [18], (f) Vo [23], (g) He [24], (h) Zhao [31], (i) Suh [27], (j) Ours.

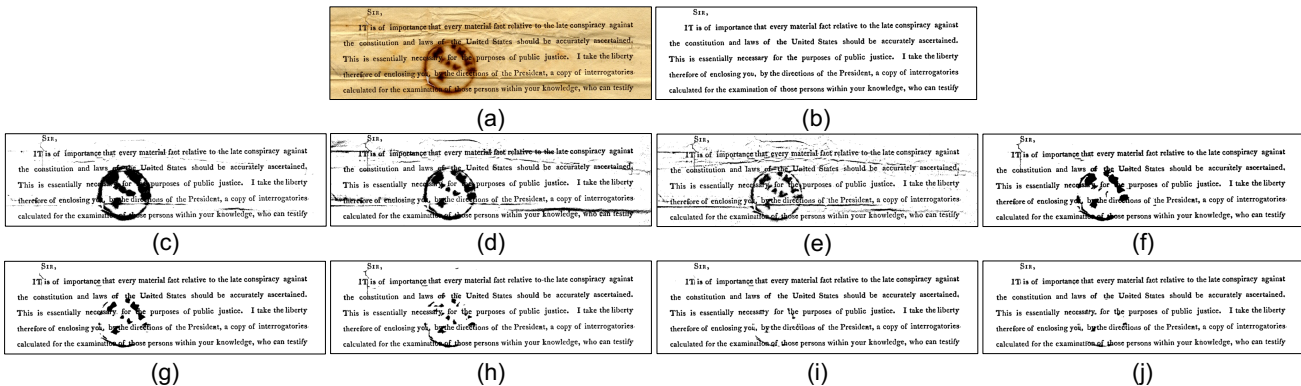


Figure 10: Example of document image binarization results from input image PR16 of DIBCO 2013 dataset by different methods: (a) original input images, (b) the ground truth, (c) Otsu [16], (d) Niblack [17], (e) Sauvola [18], (f) Vo [23], (g) He [24], (h) Zhao [31], (i) Suh [27], (j) Ours.

4.3 to compare different methods, including the traditional binarization methods employing Thresholding and SOTA methods based on CNN, Transformer, and GAN. It is important to note that not all methods were tested on these six DIBCO datasets, leading to variations in the methods compared on each dataset.

4.6. Comparison Experiment

Although the mathematical theory [37] demonstrates that the processed images can effectively retain contour information and minimize noise, we aim to comprehensively

assess the influence of these processed images on the experimental outcomes. In Stage-1, we follow the image patch size (256×256) used by the baseline model [33] and apply DWT and normalization to these image patches.

In this section, a comparison experiment is conducted to find out that whether the model would have better performance when using output images of Stage-1 with different designs as the input of Stage-2. This work utilizes UNet++ [40] architecture with EfficientNet [41] as the generator to perform the image segmentation on datasets DIBCO 2011, DIBCO 2013, H-DIBCO 2014, and H-DIBCO 2016. For the input images of the generator, three different designs

are established: (1) original input image, (2) LL subband image retained by DWT, and (3) LL subband image retained by DWT followed by normalization. For the corresponding ground truth images of the generator, except for the ground truth channel (1-D), we set three designs for the images of the other three channels, which are used in the same way as the input images.

Table 1 presents the model performances with different designs across four datasets. On these four datasets, the design that directly employs the original image as input and corresponding ground truth image provides the worst performance. Table 1 (a) indicates that the design using only DWT without normalization as input and corresponding ground truth image performs well on DIBCO 2011 dataset. Tables 1 (b) and (c) demonstrate that inputting the original images directly, and employing Stage-1 output images as the corresponding ground truth images provide the best performance on DIBCO 2013 and H-DIBCO 2014 datasets. In addition, the above design in Table 1 (d) achieves the highest p-FM value. Therefore, we choose this design to construct our network model architecture.

4.7. Ablation Study

The comparison experiments detailed in Section 4.6 demonstrates that training the generator following DWT and image normalization significantly enhances the performance of the network model. However, we would like to better demonstrate the advantages of each stage, and we have selected 5 images from PHIBD and Bickley Diary Dataset. These images are employed to systematically exhibit the results of image enhancement and binarization through the step-by-step application of different stages of our proposed method. Figure 7 (b) represents the result of retaining the LL subband images after applying DWT and normalization. This stage performs noise reduction on the original input image, which is used as the ground truth image for the generator. Figure 7 (c) shows the result of image enhancement achieved using adversarial networks, where the image has the background color removed and the color of the text highlighted. Figure 7 (d) is the final output image obtained using the proposed whole method. Notably, it is evident that our final output result closely approximates Figure 7 (e), the ground truth image.

4.8. Experimental Results

In this work, all different models are evaluated on six DIBCO datasets (DIBCO 2011, DIBCO 2013, H-DIBCO 2014, H-DIBCO 2016, DIBCO 2017, and H-DIBCO 2018). Since the DIBCO datasets do not provide OCR output, this work uses the four evaluation metrics introduced in Section 4.3 to evaluate the proposed method and other SOTA methods.

The evaluation results of the model performance on six DIBCO datasets are presented in Tables 2, 3, 4, 5, 6, 7. Among them, the FM and p-FM values of the proposed model on the DIBCO 2011 and 2013 datasets are worth noting. From Table 2, it can be seen that the FM value of our model is 94.97, which is 1.27 higher than that of the

model of Bhunia *et al.* [30] (the second highest FM value of 93.70). While the p-FM value of our model reaches 98.35 on the DIBCO 2013 dataset, which is 0.99 higher than that of the model of Suh *et al.* [27] (the second highest p-FM value of 97.36), as shown in Table 3.

Overall, the tables illustrate that the proposed method ranks the top two best performance across all evaluation metrics. However, due to variations in the rankings based on the four independent evaluation metrics, a clear representation of the model performance becomes challenging. Specifically, the overall performances of some models do not seem to be the best, but one of the four evaluation metrics has the highest value. To address this, we introduce the average metric (Avg), the specific formula for this metric is as follows:

$$Avg = (FM + p-FM + PSNR + (100 - DRD)) / 4 \quad (13)$$

It is worth noting that the proposed method achieves the highest average (Avg) value, higher than those of all other SOTA models. These results demonstrate that the proposed method achieves the SOTA overall model performance, and show that it is more efficient than the other SOTA method for binarization of degraded color documents.

In addition to assessing method performance by comparing quantitative metrics across various approaches, this study aims to provide readers with an intuitive understanding of the distinctions through application results involving images. Consequently, we have chosen images from the DIBCO 2011 and DIBCO 2013 datasets to illustrate examples of binarization outcomes. Figures 8, 9, and 10 depict the binarization results for images HW1, HW5, and PR16, utilizing diverse methodologies. These figures visually demonstrate that the proposed method outperforms the SOTA binarization method and the traditional binarization method in terms of the shadow and noise elimination. Furthermore, the proposed method is good at preserving textual content while effectively mitigating the presence of the shadows and noise.

5. Conclusion

This paper introduces a novel three-stage method based on DWT and GAN to solve the issue of text degradation in degraded document images with color backgrounds. The proposed method involves preserving the LL subband images through DWT to eliminate image noise, serving as ground truth for the generator. It trains independent networks utilizing RGB three single-channel images and one grayscale images, followed by a fusion of local and global prediction networks for binarization. As far as our knowledge extends, this work first represents the three-stage method that combines traditional image processing with deep learning. The experimental results demonstrate that employing U-Net++ with EfficientNet as the generator and PatchGAN as the discriminator outperforms performance compared to other SOTA methods.

The proposed three-stage architecture serves as a foundational framework that can be used with different networks

to train models. The utilization of advanced networks in roles such as segmentation architecture and generator encoders can notably enhance the performance of this framework. It is worth noting that self-attention mechanisms have recently stood out in computer vision tasks. In the future work, we plan to apply self-attention mechanisms to generators, aiming to attain more efficient network models and further the progress of document image binarization.

6. Declarations

This paper is an expanded paper from 20th Pacific Rim International Conference on Artificial Intelligence (PRICAI) held on November 15-19, 2023 in Jakarta, Indonesia.

6.1. Declaration of Funding

This research is supported by National Science and Technology Council of Taiwan, under Grant Number: NSTC 112-2221-E-032-037-MY2.

6.2. Declaration of competing interest

The authors have no financial or proprietary interests in any material discussed in this article.

6.3. Declaration of Generative AI and AI-assisted technologies in the writing process

The authors only use generative artificial intelligence (AI) and AI-assisted technologies to improve language.

References

- [1] R. Hedjam, M. Cheriet, Historical document image restoration using multispectral imaging system, *Pattern Recognition* 46 (8) (2013) 2297–2312.
- [2] B. Sun, S. Li, X.-P. Zhang, J. Sun, Blind bleed-through removal for scanned historical document image with conditional random fields, *IEEE Transactions on Image Processing* 25 (12) (2016) 5702–5712.
- [3] N. Kligler, S. Katz, A. Tal, Document enhancement using visibility detection, in: *Proceedings of the IEEE Conference on Computer Vision and Pattern Recognition*, 2018, pp. 2374–2382.
- [4] A. Sulaiman, K. Omar, M. F. Nasrudin, Degraded historical document binarization: A review on issues, challenges, techniques, and future directions, *Journal of Imaging* 5 (4) (2019) 48.
- [5] J. Calvo-Zaragoza, A.-J. Gallego, A selectional auto-encoder approach for document image binarization, *Pattern Recognition* 86 (2019) 37–47.
- [6] X. Peng, H. Cao, K. Subramanian, R. Prasad, P. Natarajan, Exploiting stroke orientation for crf based binarization of historical documents, in: *2013 12th International Conference on Document Analysis and Recognition, IEEE*, 2013, pp. 1034–1038.
- [7] J. Long, E. Shelhamer, T. Darrell, Fully convolutional networks for semantic segmentation, in: *Proceedings of the IEEE conference on computer vision and pattern recognition*, 2015, pp. 3431–3440.
- [8] C. Tensmeyer, T. Martinez, Document image binarization with fully convolutional neural networks, in: *2017 14th IAPR international conference on document analysis and recognition (ICDAR)*, Vol. 1, IEEE, 2017, pp. 99–104.
- [9] R.-Y. Ju, Y.-S. Lin, J.-S. Chiang, C.-C. Chen, W.-H. Chen, C.-T. Chien, Ccdwt-gan: Generative adversarial networks based on color channel using discrete wavelet transform for document image binarization, in: *20th Pacific Rim International Conference on Artificial Intelligence, PRICAI 2023, Jakarta, Indonesia, November 15–19, Springer Nature Singapore*, 2023, pp. 186–198.
- [10] I. Pratikakis, B. Gatos, K. Ntirogiannis, Icdar 2011 document image binarization contest (dibco 2011), in: *2011 International Conference on Document Analysis and Recognition, IEEE*, 2011, pp. 1506–1510.
- [11] K. Ntirogiannis, B. Gatos, I. Pratikakis, Icfhr2014 competition on handwritten document image binarization (h-dibco 2014), in: *2014 14th International conference on frontiers in handwriting recognition, IEEE*, 2014, pp. 809–813.
- [12] I. Pratikakis, B. Gatos, K. Ntirogiannis, Icdar 2013 document image binarization contest (dibco 2013), in: *2013 12th International Conference on Document Analysis and Recognition*, 2013, pp. 1471–1476. doi:10.1109/ICDAR.2013.219.
- [13] I. Pratikakis, K. Zagoris, G. Barlas, B. Gatos, Icfhr2016 handwritten document image binarization contest (h-dibco 2016), in: *2016 15th International Conference on Frontiers in Handwriting Recognition (ICFHR)*, IEEE, 2016, pp. 619–623.
- [14] I. Pratikakis, K. Zagori, P. Kaddas, B. Gatos, Icfhr 2018 competition on handwritten document image binarization (h-dibco 2018), in: *2018 16th International Conference on Frontiers in Handwriting Recognition (ICFHR)*, IEEE, 2018, pp. 489–493.
- [15] I. Pratikakis, K. Zagoris, G. Barlas, B. Gatos, Icdar2017 competition on document image binarization (dibco 2017), in: *2017 14th IAPR International Conference on Document Analysis and Recognition (ICDAR)*, Vol. 1, IEEE, 2017, pp. 1395–1403.
- [16] N. Otsu, A threshold selection method from gray-level histograms, *IEEE transactions on systems, man, and cybernetics* 9 (1) (1979) 62–66.
- [17] W. Niblack, *An introduction to digital image processing*, Strandberg Publishing Company, 1985.
- [18] J. Sauvola, M. Pietikäinen, Adaptive document image binarization, *Pattern recognition* 33 (2) (2000) 225–236.
- [19] A. Krizhevsky, I. Sutskever, G. E. Hinton, Imagenet classification with deep convolutional neural networks, *Communications of the ACM* 60 (6) (2017) 84–90.
- [20] M. D. Zeiler, R. Fergus, Visualizing and understanding convolutional networks, in: *European conference on computer vision*, Springer, 2014, pp. 818–833.
- [21] O. Ronneberger, P. Fischer, T. Brox, U-net: Convolutional networks for biomedical image segmentation, in: *International Conference on Medical image computing and computer-assisted intervention*, Springer, 2015, pp. 234–241.
- [22] X. Peng, H. Cao, P. Natarajan, Using convolutional encoder-decoder for document image binarization, in: *2017 14th IAPR international conference on document analysis and recognition (ICDAR)*, Vol. 1, IEEE, 2017, pp. 708–713.
- [23] Q. N. Vo, S. H. Kim, H. J. Yang, G. Lee, Binarization of degraded document images based on hierarchical deep supervised network, *Pattern Recognition* 74 (2018) 568–586.
- [24] S. He, L. Schomaker, Deepotsu: Document enhancement and binarization using iterative deep learning, *Pattern recognition* 91 (2019) 379–390.
- [25] I. Goodfellow, J. Pouget-Abadie, M. Mirza, B. Xu, D. Warde-Farley, S. Ozair, A. Courville, Y. Bengio, Generative adversarial networks, *Communications of the ACM* 63 (11) (2020) 139–144.
- [26] A. Konwer, A. K. Bhunia, A. Bhowmick, A. K. Bhunia, P. Banerjee, P. P. Roy, U. Pal, Staff line removal using generative adversarial networks, in: *2018 24th International Conference on Pattern Recognition (ICPR)*, IEEE, 2018, pp. 1103–1108.
- [27] S. Suh, H. Lee, P. Lukowicz, Y. O. Lee, Cegan: Classification enhancement generative adversarial networks for unraveling data imbalance problems, *Neural Networks* 133 (2021) 69–86.
- [28] P. Isola, J.-Y. Zhu, T. Zhou, A. A. Efros, Image-to-image translation with conditional adversarial networks, in: *Proceedings of the IEEE conference on computer vision and pattern recognition*, 2017, pp. 1125–1134.
- [29] M. Mirza, S. Osindero, Conditional generative adversarial nets, *arXiv preprint arXiv:1411.1784* (2014).
- [30] A. K. Bhunia, A. K. Bhunia, A. Sain, P. P. Roy, Improving document binarization via adversarial noise-texture augmentation, in: *2019*

- IEEE International Conference on Image Processing (ICIP), IEEE, 2019, pp. 2721–2725.
- [31] J. Zhao, C. Shi, F. Jia, Y. Wang, B. Xiao, Document image binarization with cascaded generators of conditional generative adversarial networks, *Pattern Recognition* 96 (2019) 106968.
- [32] R. De, A. Chakraborty, R. Sarkar, Document image binarization using dual discriminator generative adversarial networks, *IEEE Signal Processing Letters* 27 (2020) 1090–1094.
- [33] S. Suh, J. Kim, P. Lukowicz, Y. O. Lee, Two-stage generative adversarial networks for binarization of color document images, *Pattern Recognition* 130 (2022) 108810.
- [34] A. Nicolaou, V. Christlein, E. Riba, J. Shi, G. Vogeler, M. Seuret, Tormentor: Deterministic dynamic-path, data augmentations with fractals, in: *Proceedings of the IEEE/CVF Conference on Computer Vision and Pattern Recognition*, 2022, pp. 2707–2711.
- [35] M. A. Souibgui, S. Biswas, S. K. Jemni, Y. Kessentini, A. Fornés, J. Lladós, U. Pal, Docentr: An end-to-end document image enhancement transformer, *arXiv preprint arXiv:2201.10252* (2022).
- [36] R. Keys, Cubic convolution interpolation for digital image processing, *IEEE transactions on acoustics, speech, and signal processing* 29 (6) (1981) 1153–1160.
- [37] R. S. Stanković, B. J. Falkowski, The haar wavelet transform: its status and achievements, *Computers & Electrical Engineering* 29 (1) (2003) 25–44.
- [38] A. Haar, *Zur theorie der orthogonalen funktionensysteme*, Georg-August-Universität, Göttingen., 1909.
- [39] Z. Zhou, M. M. Rahman Siddiquee, N. Tajbakhsh, J. Liang, Unet++: A nested u-net architecture for medical image segmentation, in: *Deep learning in medical image analysis and multimodal learning for clinical decision support*, Springer, 2018, pp. 3–11.
- [40] Z. Zhou, M. M. R. Siddiquee, N. Tajbakhsh, J. Liang, Unet++: Redesigning skip connections to exploit multiscale features in image segmentation, *IEEE transactions on medical imaging* 39 (6) (2019) 1856–1867.
- [41] M. Tan, Q. Le, Efficientnet: Rethinking model scaling for convolutional neural networks, in: *International conference on machine learning*, PMLR, 2019, pp. 6105–6114.
- [42] C. Li, M. Wand, Precomputed real-time texture synthesis with markovian generative adversarial networks, in: *European conference on computer vision*, Springer, 2016, pp. 702–716.
- [43] J.-Y. Zhu, T. Park, P. Isola, A. A. Efros, Unpaired image-to-image translation using cycle-consistent adversarial networks, in: *Proceedings of the IEEE international conference on computer vision*, 2017, pp. 2223–2232.
- [44] C. Ledig, L. Theis, F. Huszár, J. Caballero, A. Cunningham, A. Acosta, A. Aitken, A. Tejani, J. Totz, Z. Wang, et al., Photo-realistic single image super-resolution using a generative adversarial network, in: *Proceedings of the IEEE conference on computer vision and pattern recognition*, 2017, pp. 4681–4690.
- [45] I. Gulrajani, F. Ahmed, M. Arjovsky, V. Dumoulin, A. C. Courville, Improved training of wasserstein gans, *Advances in neural information processing systems* 30 (2017).
- [46] E. R. Bartusiak, S. K. Yarlagadda, D. Güera, P. Bestagini, S. Tubaro, F. M. Zhu, E. J. Delp, Splicing detection and localization in satellite imagery using conditional gans, in: *2019 IEEE Conference on Multimedia Information Processing and Retrieval (MIPR)*, IEEE, 2019, pp. 91–96.
- [47] B. Gatos, K. Ntirogiannis, I. Pratikakis, Icdar 2009 document image binarization contest (dibco 2009), in: *2009 10th International conference on document analysis and recognition*, IEEE, 2009, pp. 1375–1382.
- [48] I. Pratikakis, B. Gatos, K. Ntirogiannis, H-dibco 2010-handwritten document image binarization competition, in: *2010 12th International Conference on Frontiers in Handwriting Recognition*, IEEE, 2010, pp. 727–732.
- [49] H. Z. Nafchi, S. M. Ayatollahi, R. F. Moghaddam, M. Cheriet, An efficient ground truthing tool for binarization of historical manuscripts, in: *2013 12th International Conference on Document Analysis and Recognition*, IEEE, 2013, pp. 807–811.
- [50] I. Pratikakis, B. Gatos, K. Ntirogiannis, Icdar 2012 competition on handwritten document image binarization (h-dibco 2012), in: *2012 international conference on frontiers in handwriting recognition*, IEEE, 2012, pp. 817–822.
- [51] F. Deng, Z. Wu, Z. Lu, M. S. Brown, Binarizationshop: a user-assisted software suite for converting old documents to black-and-white, in: *Proceedings of the 10th annual joint conference on Digital libraries*, 2010, pp. 255–258.
- [52] S. Suh, H. Lee, Y. O. Lee, P. Lukowicz, J. Hwang, Robust shipping label recognition and validation for logistics by using deep neural networks, in: *2019 IEEE International Conference on Image Processing (ICIP)*, IEEE, 2019, pp. 4509–4513.
- [53] G. D. Vo, C. Park, Robust regression for image binarization under heavy noise and nonuniform background, *Pattern Recognition* 81 (2018) 224–239.
- [54] N. R. Howe, Document binarization with automatic parameter tuning, *International journal on document analysis and recognition (ijdar)* 16 (2013) 247–258.
- [55] F. Jia, C. Shi, K. He, C. Wang, B. Xiao, Degraded document image binarization using structural symmetry of strokes, *Pattern Recognition* 74 (2018) 225–240.
- [56] Z. Yang, Y. Xiong, G. Wu, Gdb: Gated convolutions-based document binarization, *arXiv preprint arXiv:2302.02073* (2023).
- [57] W. Xiong, X. Jia, J. Xu, Z. Xiong, M. Liu, J. Wang, Historical document image binarization using background estimation and energy minimization, in: *2018 24th International Conference on Pattern Recognition (ICPR)*, IEEE, 2018, pp. 3716–3721.
- [58] S. K. Bera, S. Ghosh, S. Bhowmik, R. Sarkar, M. Nasipuri, A non-parametric binarization method based on ensemble of clustering algorithms, *Multimedia Tools and Applications* 80 (5) (2021) 7653–7673.
- [59] S. Kang, B. K. Iwana, S. Uchida, Complex image processing with less data—document image binarization by integrating multiple pre-trained u-net modules, *Pattern Recognition* 109 (2021) 107577.
- [60] S. K. Jemni, M. A. Souibgui, Y. Kessentini, A. Fornés, Enhance to read better: a multi-task adversarial network for handwritten document image enhancement, *Pattern Recognition* 123 (2022) 108370.
- [61] Y. Akbari, S. Al-Maadeed, K. Adam, Binarization of degraded document images using convolutional neural networks and wavelet-based multichannel images, *IEEE Access* 8 (2020) 153517–153534.
- [62] M. A. Souibgui, Y. Kessentini, De-gan: A conditional generative adversarial network for document enhancement, *IEEE Transactions on Pattern Analysis and Machine Intelligence* 44 (3) (2020) 1180–1191.
- [63] M. O. Tamrin, M. El-Amine Ech-Cherif, M. Cheriet, A two-stage unsupervised deep learning framework for degradation removal in ancient documents, in: *Pattern Recognition. ICPR International Workshops and Challenges: Virtual Event, January 10-15, 2021, Proceedings, Part VII*, Springer, 2021, pp. 292–303.
- [64] D. P. Kingma, J. Ba, Adam: A method for stochastic optimization, *arXiv preprint arXiv:1412.6980* (2014).
- [65] J. Deng, W. Dong, R. Socher, L.-J. Li, K. Li, L. Fei-Fei, Imagenet: A large-scale hierarchical image database, in: *2009 IEEE conference on computer vision and pattern recognition*, IEEE, 2009, pp. 248–255.

CRediT authorship contribution statement

Rui-Yang Ju : Conceptualization, Methodology, Writing – original draft. **Yu-Shian Lin** : Methodology, Data curation, Investigation. **Yanlin Jin** : Software, Validation, Writing – review & editing. **Chih-Chia Chen** : Formal Analysis, Project administration. **Chun-Tse Chien** : Visualization. **Jen-Shiun Chiang** : Funding acquisition, Supervision, Writing – review & editing.